Climatic mass balance of the ice cap Vestfonna, Svalbard: A spatially distributed assessment using ERA-Interim and MODIS data

Marco Möller,[1] Roman Finkelnburg,[2] Matthias Braun,[3,4] Regine Hock,[3,5] Ulf Jonsell,[5,6,7] Veijo A. Pohjola,[5] Dieter Scherer,[2] and Christoph Schneider[1]

Received 19 October 2010; revised 30 March 2011; accepted 22 June 2011; published 18 August 2011.

[1] The ice cap Vestfonna in the northern Svalbard archipelago is one of the largest ice bodies of the European Arctic (~2400 km^2), but little is known about its mass balance. We model the climatic mass balance of the ice cap for the period September 2000 to August 2009 on a daily basis. Ablation is calculated by a spatially distributed temperature-radiation-index melt model. Air temperature forcing is provided by ERA-Interim data that is downscaled using data from an automatic weather station operated on the ice cap. Spatially distributed net shortwave radiation fluxes are obtained from standard trigonometric techniques combined with Moderate Resolution Imaging Spectroradiometer-based cloud cover and surface albedo information. Accumulation is derived from ERA-Interim precipitation data that are bias corrected and spatially distributed as a function of elevation. Refreezing is incorporated using the P_{max} approach. Results indicate that mass balance years are characterized by short ablation seasons (June to August) and correspondingly longer accumulation periods (September to May). The modeled, annual climatic mass balance rate shows an almost balanced mean of -0.02 ± 0.20 m w.e. yr^{-1} (meters water equivalent per year) with an associated equilibrium line altitude of 383 ± 54 m above sea level (mean ± one standard deviation). The mean winter balance is $+0.32 \pm 0.06$ m w.e. yr^{-1}, and the mean summer balance -0.35 ± 0.17 m w.e. yr^{-1}. Roughly one fourth of total surface ablation is retained by refreezing indicating that refreezing is an important component of the mass budget of Vestfonna.

Citation: Möller, M., R. Finkelnburg, M. Braun, R. Hock, U. Jonsell, V. A. Pohjola, D. Scherer, and C. Schneider (2011), Climatic mass balance of the ice cap Vestfonna, Svalbard: A spatially distributed assessment using ERA-Interim and MODIS data, *J. Geophys. Res.*, *116*, F03009, doi:10.1029/2010JF001905.

1. Introduction

[2] The Arctic glaciers outside of Greenland have been found to be a major contributor to present sea level rise [e.g., *Arendt et al.*, 2002; *Berthier et al.*, 2010; *Wu et al.*, 2010]. They account for about one fourth of all glacier (excluding Greenland and Antarctica) sea level rise contributions since 1960 [*Kaser et al.*, 2006]. These contributions are expected to increase in the future [*Raper and Braithwaite*, 2006; *Meier et al.*, 2007; *Bahr et al.*, 2009], as these glaciers are located in the region of highest predicted air temperature increase during the coming decades [*Rinke and Dethloff*, 2008].

[3] During the last four decades the glaciers and ice caps of Svalbard showed a mean geodetic mass balance of -0.36 ± 0.02 m w.e. yr^{-1} (meters water equivalent per year), (excluding Austfonna and Kvitøya) corresponding to a mean sea level rise contribution of 0.026 ± 0.001 mm yr^{-1} [*Nuth et al.*, 2010]. However, their surface mass balance was roughly in equilibrium (-0.014 ± 0.003 m w.e. yr^{-1}) during the last 30 years of the 20th century [*Hagen et al.*, 2003]. Glaciers in western Svalbard have experienced an accelerating thinning during recent decades with changes in surface elevation of −0.47 and −0.62 m w.e. yr^{-1} during the periods 1995–2003 and 2003–2005, respectively [*Kohler et al.*, 2007]. These values are in line with results from the ice caps on Edgeøya, eastern Svalbard, where the thinning rate averaged −0.63 m w.e. yr^{-1} for the period 2002–2004 [*Kääb*, 2008], and results from southern Spitsbergen where mean thinning during 1990–2005 was −0.55 m w.e. yr^{-1} [*Nuth et al.*, 2010]. However, most recent estimates indicate significant changes in the mass balance pattern of the Svalbard archipelago. For the period 2003–2008,

[1]Department of Geography, RWTH Aachen University, Aachen, Germany.
[2]Department of Ecology, Technische Universität Berlin, Berlin, Germany.
[3]Geophysical Institute, University of Alaska Fairbanks, Fairbanks, Alaska, USA.
[4]Center for Remote Sensing of Land Surfaces, University of Bonn, Bonn, Germany.
[5]Department of Earth Sciences, Uppsala University, Uppsala, Sweden.
[6]Escuela Técnica Superior de Ingenieros de Telecomunicación, Universidad Politécnica de Madrid, Madrid, Spain.
[7]Now at Swedish Polar Research Secretariat, Stockholm, Sweden.

0148-0227/11/2010JF001905

Moholdt et al. [2010b] calculated the overall geodetic mass balance to be much less negative at -0.11 ± 0.04 m w.e. yr^{-1}.

[4] Results for Vestfonna are close to the regional mean (-0.14 ± 0.07 m w.e. yr^{-1}), while a much more positive balance of $+0.1 \pm 0.04$ m w.e. yr^{-1} was obtained for Austfonna for the same period [*Moholdt et al.*, 2010b]. Positive mass balances for Austfonna have also been reported for the end of the 20th century [*Bevan et al.*, 2007]. For Vestfonna *Nuth et al.* [2010] obtained a near zero glacier-wide geodetic mass balance of $+0.05 \pm 0.15$ m w.e. yr^{-1} for the period 1990–2005 and a thickening of parts of its accumulation area.

[5] Hence, Vestfonna seems to have shifted from slight mass gain to mass loss. Vestfonna does not experience the typical low-elevation thinning observed throughout the Svalbard archipelago. Rather, it features a complex pattern of ice thickness changes [*Moholdt et al.*, 2010b] due to the relatively complex surface topography of Vestfonna when compared to the smoother surface of Austfonna.

[6] With the exception of Austfonna, the negative mass balance observations agree with the positive trends of air temperature observed in the Arctic and the Svalbard area in particular [*Rigor et al.*, 2000; *Moritz et al.*, 2002]. In general, the archipelago experienced warming during the 20th century [e.g., *Hanssen-Bauer and Førland*, 1998; *Førland and Hanssen-Bauer*, 2003]. During the last decades of the 20th century, the Atlantic sector of the Arctic as a whole showed the strongest warming trend of any part of the northern polar region [*Przybylak*, 2000; 2007]. During the period 2001–2005, the mean annual air temperature in the Atlantic sector of the Arctic was 1.3 K higher than its long-term mean during 1951–1990 [*Przybylak*, 2007]. This development led to a considerable increase of the mean length of annual melt season throughout the Arctic [*Stroeve et al.*, 2006b], and thus possibly initiated a trend toward more negative mass balances.

[7] The aim of this study is to model daily fields of surface accumulation, surface ablation, refreezing, and their sum, the so-called climatic mass balance of Vestfonna for the first decade of the 21st century (September 2000 to August 2009). We apply the spatially distributed temperature-radiation-index ablation model presented by *Pellicciotti et al.* [2005] that is based on air temperature and net shortwave radiation inputs. We enhance the model by including fractional cloud cover and albedo fields derived from daily MODIS (Moderate Resolution Imaging Spectroradiometer) imagery in order to compute net shortwave radiation. The model is forced by statistically downscaled ERA-Interim daily air temperatures. Local reference is provided by records of automatic weather stations (AWS) operated in the study area. Accumulation is modeled as a function of altitude based on ERA-Interim daily total precipitation. Our model approach accounts for the frequent and spatially variable cloud cover in the study area, despite the limited availability of meteorological data at boundary layer level. Model results provide new insight into the spatial and temporal variability of the surface mass balance of Svalbard's second largest ice cap.

2. Study Area

[8] Vestfonna is a polythermal ice cap located on the island Nordaustlandet (northernmost Svalbard archipelago) at around 80°N (Figure 1). It covers ~2400 km^2 making it one of the largest ice masses of the European Arctic. It ranges in altitude from sea level to 630 m above sea level (asl). The ice cap has a main ridge that is oriented east-west, with its second highest point, called Ahlmann Summit, located near the center. Another main ridge extends northward from a slightly higher peak located in the eastern part of the ice cap. Between these ridges, Vestfonna has pronounced, bowl-shaped outlet glacier basins. Some of these outlet glaciers have been suggested to be surge-type glaciers [*Dowdeswell and Collin*, 1990], although this has not yet been proven.

[9] The majority of the ice cap drains southward into Wahlenbergfjorden through large (>5 km wide) calving fronts [*Strozzi et al.*, 2008]. The largest outlet glacier, Franklinbreen, is located on the northwestern side of the ice cap and drains into Lady Franklinfjorden. A few smaller outlet glaciers drain into northeastern fjords.

[10] Svalbard features a maritime climate characterized by cooler summers and warmer winters than generally found at comparable latitudes. Mean monthly air temperatures on Vestfonna during the short summer seasons do not exceed +3°C and in winter they typically range between −10°C and −15°C. Periods of considerable short-term warming with air temperatures rising close to the melting point frequently occur, even during the winter months (Figure 2).

[11] The location of Vestfonna in the northeastern part of Svalbard causes the ice cap to be more directly influenced by weather systems originating in the Barents Sea region than by the westerly weather systems that determine the climate of other parts of the archipelago [*Taurisano et al.*, 2007]. Accordingly, the ice-free areas of the Barents Sea form the major source of moisture for precipitation over Nordaustlandet [*Førland et al.*, 1997]. However, as Vestfonna is situated in the lee of its higher-elevation neighbor, Austfonna, it receives less precipitation and has a smaller horizontal precipitation gradient than Austfonna [*Taurisano et al.*, 2007].

3. Data

[12] The model requires elevation data of the ice-cap surface as well as daily air temperature and precipitation data. Fractional cloud cover, atmospheric turbidity and albedo data are used to compute net shortwave radiation. Mass balance data that are obtained from ablation-stake measurements are used to calibrate the model.

3.1. Glacier Outline and Elevation Data

[13] The glacier outlines were digitized from Terra ASTER (Advanced Spaceborne Thermal Emission and Reflection Radiometer) imagery acquired on 17 August 2000 (EOS Data Gateway Granule ID: SC:ASTL1B 00-08-12:36:0010269001). Terrain information is based on the elevation data set of the ASTER Global Digital Elevation Model (GDEM). Small data gaps in the uppermost parts of the ice cap were filled with values interpolated from surrounding grid cells. Sporadic elevation outliers along the ridges were likewise substituted with interpolated values. The original grid was then bilinearly resampled to a grid-cell resolution of 250 × 250 m to facilitate coregistration with the MODIS data sets.

3.2. Meteorological Data

[14] The model is forced by statistically downscaled daily ERA-Interim 2 m air temperatures and daily ERA-Interim total precipitation (Figure 2). ERA-Interim is the follow-up

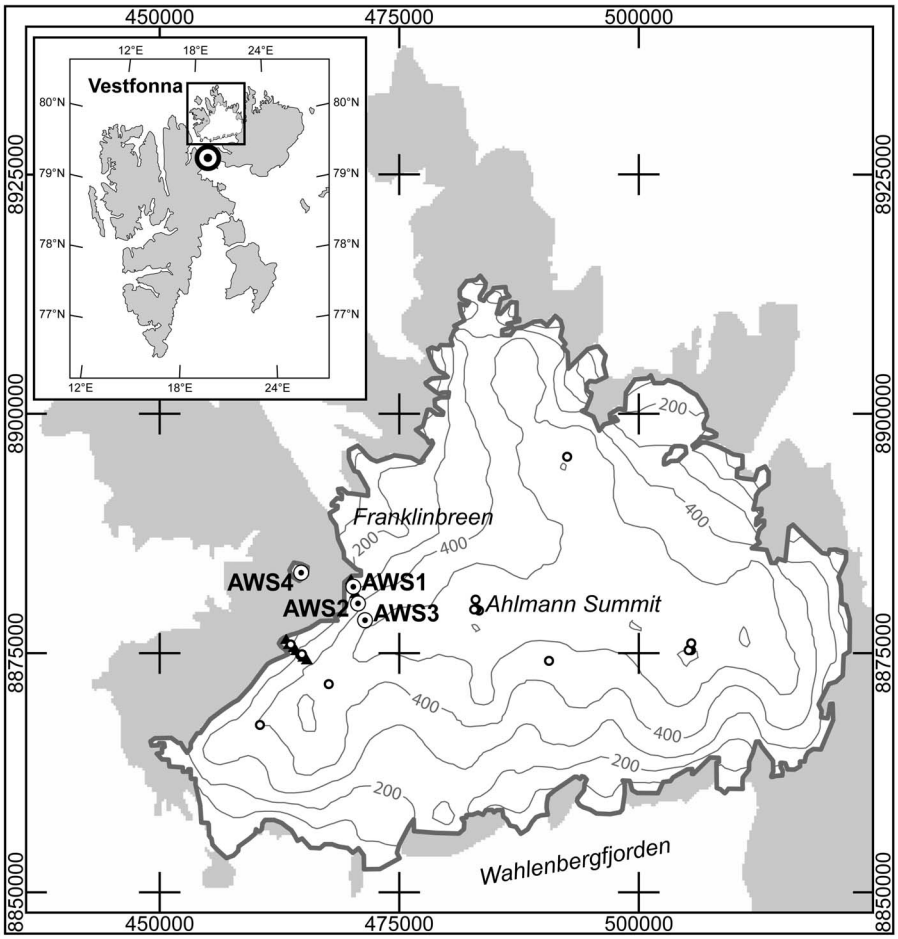

Figure 1. Location of the ice cap Vestfonna and overview on installed measurement network. The four AWSs are marked by large black circles. Locations of stakes are marked by small triangles, and locations of snow pits are marked by small circles. Locations along the transect AWS1-3 are hidden behind the AWSs marks. Contour spacing is 100 m. Coordinates correspond to Universal Transverse Mercator (UTM) zone 34N. Inset: Location of Vestfonna within Svalbard archipelago. Black circle marks the location of the ERA-Interim grid point.

reanalysis product of the well-established ERA-40 data set [*Uppala et al.*, 2005]. Data are supplied by the European Centre for Medium-Range Weather Forecasts (ECMWF). We use data from the grid point located at 79.5°N 19.5°E (Figure 1). The downscaling procedure for air temperature data is detailed in section 4.5.

[15] In addition, data from four automatic weather stations (AWS) operated on the northwestern side of the ice cap and on neighboring De Geerfonna (Figure 1) during the period 27 May 2008 to 30 April 2010 are used to downscale ERA-Interim air temperatures, to derive temperature slope lapse rates, and to calibrate the radiation model (Table 1).

[16] The air temperature records of AWS2 show data gaps in the winter seasons due to power shortage. They were filled by linearly scaled data ($R^2 = 0.97$) of the AWS on De Geerfonna (AWS4) in order to provide a continuous local reference during air temperature downscaling. However, short gaps without any air temperature data remain in May 2009 and March 2010. The time series is nevertheless considered an adequate local reference for downscaling as in this study air temperature accuracy is by far most important during the summer seasons.

3.3. Albedo

[17] Terra MODIS data were used for retrieval of daily albedo fields of Vestfonna. Albedo information is based on the daily updated MODIS snow product MOD10A1 version 5 [*Hall et al.*, 2002; *Hall and Riggs*, 2007] with a spatial resolution of 500 m. Daily albedo information is based on the scene acquired closest to nadir relating to each individual pixel. Where no MODIS albedo information is available due to cloud cover, the albedo time series at that grid point is interpolated between the temporally closest data values available.

[18] During polar winter, when no MODIS snow cover data are available (25 October to 15 February), the entire ice cap is assumed to be covered with snow having a constant albedo of 0.80. Mean update interval for albedo over the ice cap is 2.9 ± 10.8 days for the period of available MODIS snow cover, with the given range indicating one standard deviation and thus a strongly asymmetric distribution.

[19] On the southern outlet glacier tongues of the ice cap, small areas of permanent data gaps are present in the MODIS snow product (26.25 km^2). Surface albedo throughout these

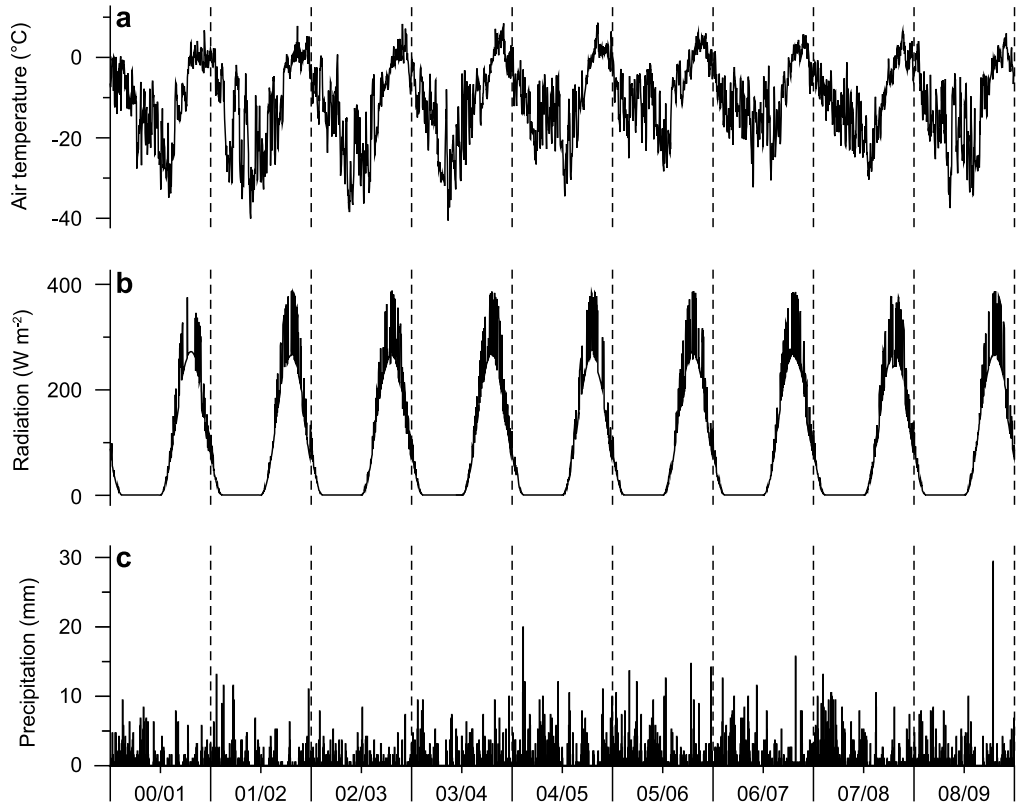

Figure 2. Climate data time series for mass balance years 2000/2001 to 2008/2009: (a) downscaled ERA-Interim air temperature, (b) modeled global radiation, and (c) scaled ERA-Interim precipitation sums. All data are presented at a daily resolution and refer to the location of AWS2 (see Figure 1). Annual subdivisions on the *x* axis start September 1.

areas was extrapolated based on the albedo of neighboring grid cells.

[20] Comparison of remotely sensed surface albedo with the measurement record of AWS2 yield a mean difference of +0.02 over the period May 2008 to July 2009 and a root mean square error (RMSE) of 0.12. This result is in agreement with uncertainties obtained by *Greuell and Oerlemans* [2005] on the Greenland ice sheet and is regarded as an adequate reproduction of in situ conditions, given that the AWS only samples a small point within the much larger MODIS footprint [*Stroeve et al.*, 2006a]. A characteristic annual evolution of the albedo bias depending on solar zenith angle as described by *Wang and Zender* [2010] is not clearly identifiable due to the limited length of the study period. Therefore, a systematic correction of the albedo fields was not feasible, and uncertainty of unknown magnitude is introduced to modeled climatic mass balances.

3.4. Fractional Cloud Cover

[21] Daily fractional cloud cover fields over Vestfonna were created on the basis of the MOD10A1 daily snow product and serve as input for the global radiation computation. Binary cloud cover information is contained by default in this 500 m resolution gridded data set. MODIS cloud cover information has been widely used in several studies and was successfully validated over snow covered ground [e.g., *Berendes et al.*, 2004; *Wang et al.*, 2008].

[22] Preprocessed fractional cloud cover fields are provided by the MODIS cloud product (MOD06_L2), but only on a 5 km spatial resolution. These fields are created by averaging the binary cloud cover information (1 km) of fixed 5 × 5 pixel subsets. We customized this method to obtain fractional cloud cover fields at the same 500 m resolution as the MOD10A1 input data. A running 5 × 5 pixel window is used to calculate fractional cloud cover for the respective central pixel. During polar night, when no MOD10A1 data are available (25 October to 15 February) and incoming shortwave radiation is negligible, fractional cloud cover is assumed to be 0 throughout the entire model domain.

3.5. Atmospheric Turbidity

[23] Atmospheric turbidity data needed for radiation modeling are represented by the Linke turbidity factor [*Linke*, 1961]. The Solar Radiation Database SoDa [*Wald et al.*, 2002] provides mean monthly values of the Linke turbidity factor on a 0.5° global grid. It is a standard tool among solar engineering

Table 1. Metadata of Automatic Weather Stations[a]

Station	Altitude (m asl)	Period
AWS1	240	23 May 2008–30 Apr 2009
AWS2	370	29 May 2008–30 Apr 2010
AWS3	500	22 May 2008–30 Apr 2009
AWS4	240	27 May 2008–30 Apr 2010
Variable at AWS1-4	sensor	accuracy
Air temperature	Campbell CS215	±0.9°C
Shortwave radiation	Campbell CS300	±5%

[a]All four AWS recorded air temperature and incoming and reflected shortwave radiation.

Table 2. Overview of Model Parameters. *dT/dz* Is Air Temperature Slope Lapse Rate

Parameter	Value and Unit	Equation
m, n	0.0000099, 0.0079	1
f_T	1.394 mm w.e. K^{-1} day^{-1}	2
f_R	0.098 mm w.e. W^{-1} m^2 day^{-1}	2
o_1, p_1	−2.73°C, 1.10	3
o_2, p_2	−4.26°C, 0.90	3
o_3, p_3	−1.79°C, 1.05	3
o_4, p_4	−3.34°C, 1.00	3
o_5, p_5	−3.37°C, 1.08	3
o_6, p_6	−2.70°C, 1.30	3
o_7, p_7	−2.30°C, 1.20	3
o_8, p_8	−4.00°C, 2.01	3
o_9, p_9	−2.96°C, 1.26	3
o_{10}, p_{10}	−2.57°C, 1.06	3
o_{11}, p_{11}	−3.10°C, 1.02	3
o_{12}, p_{12}	−2.74°C, 1.02	3
q, r	0.0, 0.364	9, 10
dT/dz	−7.0 K km^{-1}	n.a.

professionals and a widely used data provider for various solar radiation modeling applications [e.g., *Schüttemeyer et al.*, 2007]. Grids of monthly values were downloaded from the database (http://www.soda-is.com) and resampled to the 250 m resolution model domain.

3.6. Mass Balance Data

[24] Measurements of snow depth and ice surface height changes used for calibration of the mass balance model were carried out at a network of ablation/accumulation-stakes consisting of 15 stakes distributed over parts of the ablation area of the ice cap (Figure 1). We do not use stake data from the accumulation area because the amount of refreezing is not measured. A total of 29 successful repeat readings were retrieved during several field campaigns in 2007, 2008, and 2009. Measurement intervals are grouped into two major classes, that is, 70–90 days (between spring and summer campaigns) and 270 days (between summer and spring campaigns).

[25] Measurements of snow water equivalent and bulk snow densities were carried out in 21 snow pits distributed across the ice cap (Figure 1) [*Möller et al.*, 2011]. Data were used for calibration of the accumulation model and for conversion of repeat stake measurements into water equivalent values. A mean bulk snow density of 398 ± 41 kg m^{-3} (mean ± one standard deviation) was obtained from the snow pits. Density showed a low variability in space and time, which is explained by continuous compaction of the snowpack throughout the year due to frequent snowdrift [*Goodison et al.*, 1981]. Accordingly, all snow-related mass balance measurements are converted into water equivalent value using a single snow density (400 kg m^{-3}). Ice density is set to 900 kg m^{-3} [*Paterson*, 1994].

4. Model Description and Calibration

4.1. Mass Balance Model

[26] Our mass balance model computes surface accumulation, surface ablation and refreezing as well as their sum, the so-called climatic mass balance, following the terminology by *Cogley et al.* [2011]. Ablation (defined as negative in case of mass loss) is calculated as a function of downscaled ERA-Interim air temperature data and modeled net shortwave radiation. Accumulation is derived from ERA-Interim precipitation data that are distributed as a function of elevation. Refreezing is estimated using the P_{max} approach [*Reeh*, 1991].

[27] Modeling is done for the 9-year period from September 2000 until August 2009 with a daily resolution on a 250 m grid. Calibration is based on point balance data provided by repeat stake readings and snow pit data.

4.2. Accumulation

[28] Surface accumulation is assumed to be exclusively formed by snowfall. All precipitation occurring at air temperatures below 0°C is assumed to fall as snow, while rain is assumed for all precipitation at temperatures above 2°C. Between 0 and 2°C, a mixture of snow and rain is assumed, and the amount of snowfall is scaled between 100% (0°C) and 0% (2°C) using a hyperbolic function [*Möller et al.*, 2007]. Initial snowfall fields are calculated from daily ERA-Interim total precipitation of a grid point south of Vestfonna (Figure 1) by using the air temperature fields described in section 4.5.

[29] *Möller et al.* [2011] have shown a strong increase of surface accumulation with altitude. Here we approximate surface accumulation (c) from the initial snowfall fields (S_{ERA}) by quadratic scaling according to an index function of altitude (z):

$$c(z) = S_{ERA}\left(mz^2 + nz + 1\right). \quad (1)$$

The coefficients m and n (Table 2) of this index function are determined empirically (Figure 3) from in situ measurements of snow water equivalent in 16 snow pits across the ice cap [*Möller et al.*, 2011]. For each snow pit location, index values are calculated as the ratio of the sum of snow pit-derived surface accumulation close to the end of the winter season and the corresponding snowfall sum obtained from the initial ERA-Interim snowfall fields.

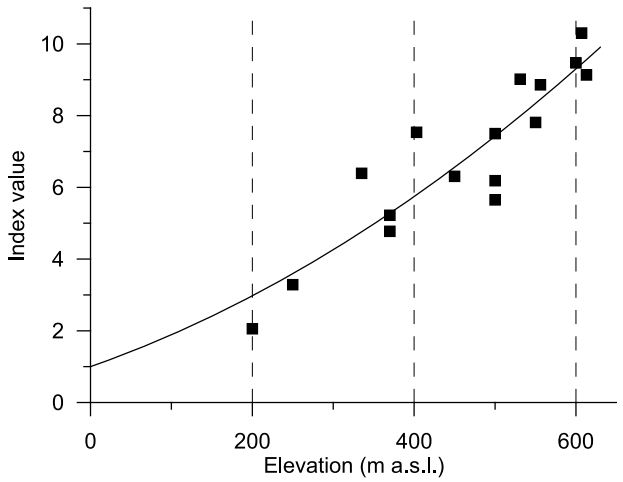

Figure 3. Index function for distribution of accumulation with altitude. Individual index values are marked as black squares. The black line is the fitted index function given in equation (1).

[30] A quadratic accumulation index function defined by m and n is fitted to the set of individual index values (Figure 3). The intercept of the index function is forced to 1.0, as surface accumulation is assumed to be equal to ERA-Interim snowfall at sea level. The relation between index values and elevation holds for all four accumulation seasons included in the data (2006/2007 to 2009/2010).

[31] The fitted index function explains 83% of the variance of the individual index values. Considerable parts of the remaining deviations (RMSE = 0.94) can be attributed to local scale snow depth variability induced by frequent formation of flat, small scale surface roughness (sastrugi). According to the index function, surface accumulation on Vestfonna increases by a factor of more than eight from the margin to the top of the ice cap. Modeled surface accumulation thus resembles magnitudes and gradients previously reported for Austfonna [*Schuler et al.*, 2007; *Taurisano et al.*, 2007].

4.3. Refreezing

[32] Refreezing in snow and firn plays a major role in the mass budget of Arctic glaciers [e.g., *Palosuo*, 1987]. In this study, it is accounted for by applying the well-established $P_{\max}$ modeling approach introduced by *Reeh* [1991]. $P_{\max}$ is calculated as a fraction of winter accumulation. It represents the maximum meltwater amount that can refreeze within the snowpack during the following ablation season before runoff occurs. It thus adds a positive value to glacier mass balance. As done by *Schuler et al.* [2007] for Austfonna, we set $P_{\max}$ = 0.6. Hence, melt and rainwater are retained by refreezing processes until 60% of the current year's winter accumulation is reached. Any excess water is assumed to be lost from the glacier as runoff.

4.4. Ablation

[33] Surface ablation, that is, snow or ice melt, is calculated using a combined temperature-radiation-index approach. Since it only depends on air temperature and surface type as input variables, the temperature-index method [e.g., *Hock*, 2003] is a useful melt modeling approach in regions with limited data availability [e.g., *Braithwaite and Raper*, 2007; *Möller and Schneider*, 2010]. It is justified by the fact that incoming long wave radiation and sensible heat flux, which usually represent the largest energy sources for snow and ice melt, are strongly correlated to air temperature [*Ohmura*, 2001].

[34] We use the temperature-radiation-index model developed by *Pellicciotti et al.* [2005], which parameterizes snow and ice ablation as

$$a = f_T T + f_R(1-\alpha)R_G \text{ for } T > 0^\circ\text{C} \tag{2}$$

$$a = 0 \text{ for } T \leq 0^\circ\text{C},$$

where a is ablation, T is air temperature, and R_G is global radiation. α is albedo, and f_T and f_R are empirical coefficients.

[35] Spatially distributed global radiation is modeled using the radiation model described in section 4.6. The amount of global radiation absorbed at the surface is determined using the MODIS-based albedo fields (see section 3.3).

4.5. Air Temperature

[36] ERA-Interim daily 2 m air temperatures from a grid point south of Vestfonna (Figure 1) were statistically downscaled to match local conditions at Vestfonna using the variance-inflation method [*Karl et al.*, 1990; *Huth*, 1999].

[37] The variance-inflation method was developed for downscaling of global circulation model data, in order to make its variance match the one at local scale. It implicitly assumes local variability to be entirely governed by synoptic scale forcing [*von Storch*, 1999], but was nevertheless considered to be an appropriate tool for reproduction of day-to-day variability in local scale air temperature data [*Huth et al.*, 2001]. Reanalysis data such as those used in this study represent an interpolated local scale and are thus based on measurements and observations. We therefore consider variance inflation to be an appropriate tool for downscaling of ERA-Interim air temperatures to Vestfonna local conditions.

[38] The downscaling follows a two-step approach [*von Storch*, 1999]. It is done separately for each month i in order to account for the strong interannual variability of air-temperature variance at the study site, that is, small variance in summer and high variance in winter. First, the synoptic scale data ($T_{\mathrm{ERA},i}$) are linearly adjusted to local scale conditions at Vestfonna according to

$$\hat{T}_{\mathrm{ERA},i} = o_i + p_i T_{\mathrm{ERA},i}. \tag{3}$$

The coefficients o_i and p_i (Table 2) are determined from linear regression analysis between ERA-Interim and AWS2 data. Then, the variance of the adjusted air temperatures is inflated to match the one observed at AWS2:

$$T_i = \sqrt{\frac{\mathrm{var}\left(T_{\mathrm{AWS2},i}\right)}{\mathrm{var}\left(\hat{T}_{\mathrm{ERA},i}\right)}}\hat{T}_{\mathrm{ERA},i}. \tag{4}$$

The downscaled air temperature time series (Figure 2) shows RMS errors of 0.7 K (June to August) and 1.2 K (September to May), when compared to measurements at AWS2.

[39] Air temperature fields are created using a constant linear lapse rate (dT/dz, Table 2). This average lapse rate is obtained from daily mean air-temperature data of AWS1–3 during the period June 2008–April 2009. Results suggest a value of 7.0 ± 3.7 K km^{-1}, with the given range indicating one standard deviation.

4.6. Global Radiation

[40] Global radiation (R_G) is calculated as the sum of solar radiation ($R_{S,\mathrm{sol}}$) and multiple scattering and reflection between the glacier and the lowermost cloud layers ($R_{S,\mathrm{msr}}$):

$$R_G = R_{S,\mathrm{sol}} + R_{S,\mathrm{msr}}. \tag{5}$$

[41] All shortwave radiation fluxes are computed with an hourly resolution from which daily means are computed.

4.6.1. Solar Radiation

[42] Potential clear-sky direct solar radiation on an arbitrarily oriented and inclined surface ($R_{0,\mathrm{sol}}$) is estimated according to *Bernhardt and Philipps* [1958] and *Mölg et al.* [2003]:

$$R_{0,\mathrm{sol}} = S_0 E \cos\zeta * \left[\frac{0.907}{(\cos\zeta)^{0.018}}\right]^{\frac{T_L}{\cos\zeta}}. \tag{6}$$

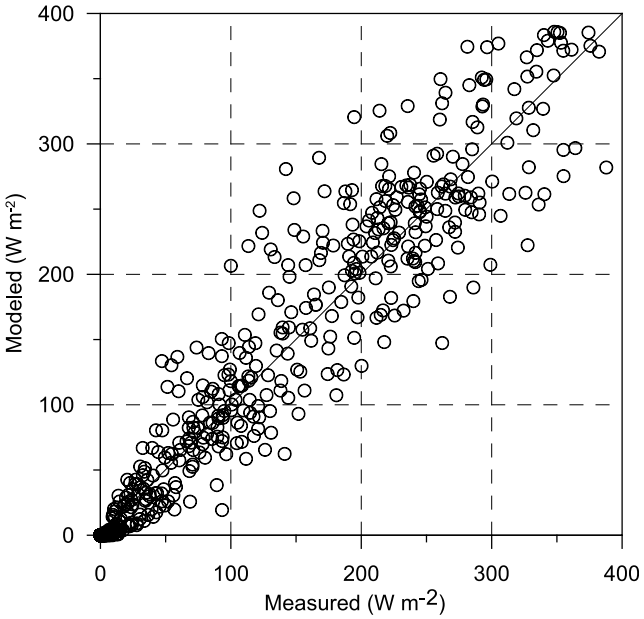

Figure 4. Modeled versus measured daily global radiation at AWS2 in the period May 2008 to April 2010.

S_0 is the solar constant (1368 W m^{-2}). Eccentricity correction factor (E) and zenith angle of the sun with respect to a theoretical, planar surface (ζ) or with respect to an arbitrarily oriented and inclined surface (ζ^*) are calculated according to standard solar geometry [e.g., *Iqbal*, 1983]. Atmospheric turbidity is represented by spatially distributed grids of the Linke turbidity factor (T_L) [*Linke*, 1961]. Terrain shading is taken into account using standard algorithms of solar-radiation geometry [*Corripio*, 2003].

[43] The reduction of clear-sky solar radiation due to actual cloud-cover conditions is determined from $R_{0,\mathrm{sol}}$ using the Savinov-Ångström formula [e.g., *Kondratyev*, 1969]. The portion of clear-sky solar radiation actually reaching the surface ($R_{S,\mathrm{dir}}$) is thus calculated as

$$R_{S,\mathrm{sol}} = R_{0,\mathrm{sol}}\left[1 - (1 - \eta')C_{fc}\right]. \tag{7}$$

Cloudiness is incorporated in terms of spatially distributed fractional cloud cover grids (C_{fc}) and η' is an empirical coefficient being 0.58 at 80°N [*Budyko*, 1974]. This implies that under completely overcast conditions (C_{fc} = 1) $R_{S,\mathrm{sol}}$ amounts to 58% of clear-sky solar radiation. Due to the minimal input requirements, the Savinov-Ångström formula (equation (7)) is a feasible method for efficient radiation calculation and has thus been used before in several studies [e.g., *Emelyanov and Konovalov*, 1975; *Dumanskaya*, 2008].

4.6.2. Multiple Scattering and Reflection

[44] Multiple scattering and reflection between the glacier and the lowermost cloud layers is an important component of global radiation at the surface [*Ørbæk et al.*, 1999]. Reflected shortwave radiation from surrounding topography is assumed to be negligible in this study, as the roughly convex shape of the ice body and the resulting lack of surrounding surfaces do not allow for reflections toward the ice cap.

[45] The radiation flux due to multiple scattering and reflection ($R_{S,\mathrm{msr}}$) is calculated from direct radiative forcing according to

$$R_{S,\mathrm{msr}} = R_{S,\mathrm{sol}} s_R. \tag{8}$$

The spatially distributed scaling factor (s_R) that accounts for surface albedo and fractional cloud-cover conditions is empirically calibrated from a comparison of measured and modeled global radiation fluxes at AWS2 in the period from 28 May 2008 to 6 August 2009. It is given by

$$s_R = q + r\alpha C_{fc}\frac{SV}{SV_{\mathrm{AWS2}}}, \tag{9}$$

and depends largely on surface albedo (α) and fractional cloud cover (C_{fc}). Differences in sky-view factors (SV) between any location on the glacier and the calibration site (AWS2) are taken into account by the given quotient ($SV_{\mathrm{AWS2}} = 0.88$). Sky-view factors are computed according to *Corripio* [2003]. The scaling factor s_R is thus a gridded quantity whose spatial distribution depends on daily updated albedo and fractional cloud cover grids and a fixed distribution of sky-view factors. The regression constants (q, r; Table 2) are calibrated from a comparison of measured global radiation (R_{meas}) and modeled ($R_{S,\mathrm{dir}}$) solar radiation at AWS2 using the following equation:

$$\frac{R_{\mathrm{meas,AWS2}} - R_{S,\mathrm{sol,AWS2}}}{R_{S,\mathrm{sol,AWS2}}} = q + r\alpha_{\mathrm{AWS2}} C_{fc,\mathrm{AWS2}}. \tag{10}$$

The difference given in the numerator, that is, the deviation of modeled from measured values, is treated as radiation fluxes originating in multiple scattering and reflection ($R_{S,\mathrm{msr}}$). Hence, the left side of equation (10) represents the ratio between multiple scattering and reflection and direct radiation fluxes at AWS2, and therefore with s_R. The constant r is obtained using linear regression techniques. With the product of albedo and fractional cloud cover ranging between 0 and 1, this means that multiple scattering and reflection at AWS2 might contribute more than one fourth to global radiation. The intercept q is forced to 0 in order to account for the fact that multiple scattering and reflection do not exist where either albedo or fractional cloud cover are zero.

[46] Modeled global radiation fluxes are able to explain 90% of the variance of in situ measurements at AWS2 (Figure 4), and considerable parts of the remaining deviations (RMSE = 36.1 W m^{-2}) can be attributed to intraday changes in cloud cover. This high temporal resolution is not provided in the MODIS-based fractional cloud cover data as it only represents samples at the overpass times of the Terra satellite.

[47] Alternative tests considering a spatially or temporally averaged cloud cover over Vestfonna resulted in a considerably diminished performance of the radiation model. Modeling attempts using the preprocessed 5 km MODIS fractional cloud cover fields led to slightly higher deviations between measured and modeled global radiation fluxes.

4.7. Model Calibration

[48] The calibration of the mass balance model is based on point balances at the stake network. Calibration is done by adjusting the empirical coefficients f_T and f_R of the ablation

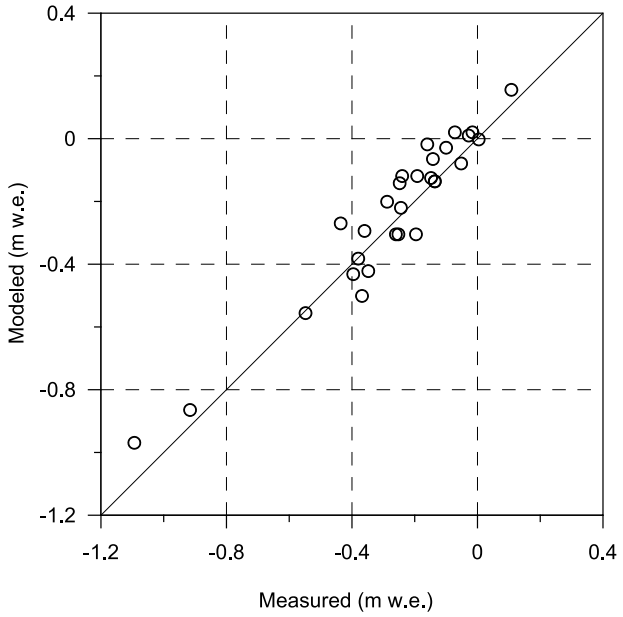

Figure 5. Modeled versus measured point climatic mass balances at the stakes (Figure 1) in the period 2007–2009.

model. Iterative mass balance model runs with continuous changes of f_T and f_R are performed until a best fit approximation between modeled point balances and their measured counterparts is reached, using RMSE minimization (Table 2). The modeled point balances account for an explained variance of 86% of the stake measurements (Figure 5). The RMSE between modeled and measured values is ±0.10 m w.e. Both the spatial and temporal variability in mass balance is reproduced well by the model.

5. Model Uncertainty

[49] The overall uncertainty of the modeled climatic mass balances time series (U_b) is quantified by accounting for errors inherent in the input data and in calibrated model parameters. We include seven individual errors (Table 3) that are assumed to be uncorrelated to each other. The overall uncertainty is thus calculated as

$$U_b = \sqrt{\sum_{i=1}^{7} U_i^2} \tag{11}$$

by applying error propagation rules [*Bevington*, 1969]. U_b is calculated on a monthly basis (Figure 6) by performing additional model runs with input data or model parameters altered according to the individual error ranges (Table 3).

[50] Uncertainty originating from air temperature inputs (U_1) is accounted for by the RMSE between downscaled ERA-Interim data and measurements at AWS2. Different values for ablation and accumulation seasons are given as the distinctly different variances of air temperatures in summer and winter lead to similarly different downscaling accuracies. The uncertainty of the temperature lapse rate (U_2) is accounted for by its measured standard deviation.

[51] Uncertainty originating from global radiation inputs (U_3) is assessed from the RMSE between modeled values and measurements at AWS2. The inaccuracy of the albedo fields (U_4) is incorporated by accounting for the RMSE between measurements at AWS2 and MODIS data of the respective grid cell.

[52] The variability of snow density results in uncertainty ranges of the temperature and radiation factors of the ablation model during calibration (U_5). It is incorporated using the standard deviation of measured bulk snow densities [*Möller et al.*, 2011].

[53] Uncertainties induced by the accumulation model (U_6) are accounted for considering the RMSE of the fitted accumulation-index function (Figure 3). It is incorporated by constant shifts of the function along the intercept according to the RMSE value. The uncertainty within the calculation of refreezing (U_7) is estimated by applying alternative values for the assumed P_{max} fraction, that is, 0.5 and 0.7.

[54] The overall model uncertainty shows distinct differences between summer (June to August) and winter (September to May) seasons (Figure 6). Monthly errors in summer are found to be about nine times higher than in winter. The mean monthly error range in summer is ±0.062 m w.e. and shows high intermonthly variability (standard deviation of ±0.034 m w.e.). Error ranges in the winter months show a mean of only ±0.007 m w.e. with only small intermonthly variability (standard deviation of ±0.005 m w.e.).

[55] This temporal pattern is due to the fact that uncertainty in ablation calculation exceeds that of accumulation and refreezing calculation (Figure 6). The mean annual error range of calculated ablation sums up to ±0.18 m w.e. while that of accumulation and refreezing only amount to ±0.07 m w.e. and ±0.04 m w.e., respectively (Table 4). This is because most of the uncertainties considered predominantly affect ablation. The uncertainties inherent in the albedo fields and the downscaled air temperature data have the greatest impact on overall model uncertainty. Overall, the uncertainty analysis suggests that the model is sufficiently robust to assess the climatic mass balance of Vestfonna.

6. Results and Discussion

[56] In the period 2000–2009, the modeled surface mass balance regime of the ice cap is characterized by long accumulation periods (September to May) and short ablation periods (June to August, Figure 6). Model results reveal a mean climatic mass balance rate of -0.02 ± 0.20 m w.e. yr^{-1}

Table 3. Overview of Uncertainties of Model Parameters[a]

Variable	Parameter	Value
U_1	air temperature	±0.7 K (abl. period) ±1.2 K (acc. period)
U_2	*dt/dz*	±3.7 K km^{-1}
U_3	global radiation	±36.1 W m^{-2}
U_4	albedo	±0.12
U_5	snow density	±40 kg m^{-3}
U_6	accumulation index	±0.94
U_7	refreezing (P_{max})	±0.1

[a]See equation (11).

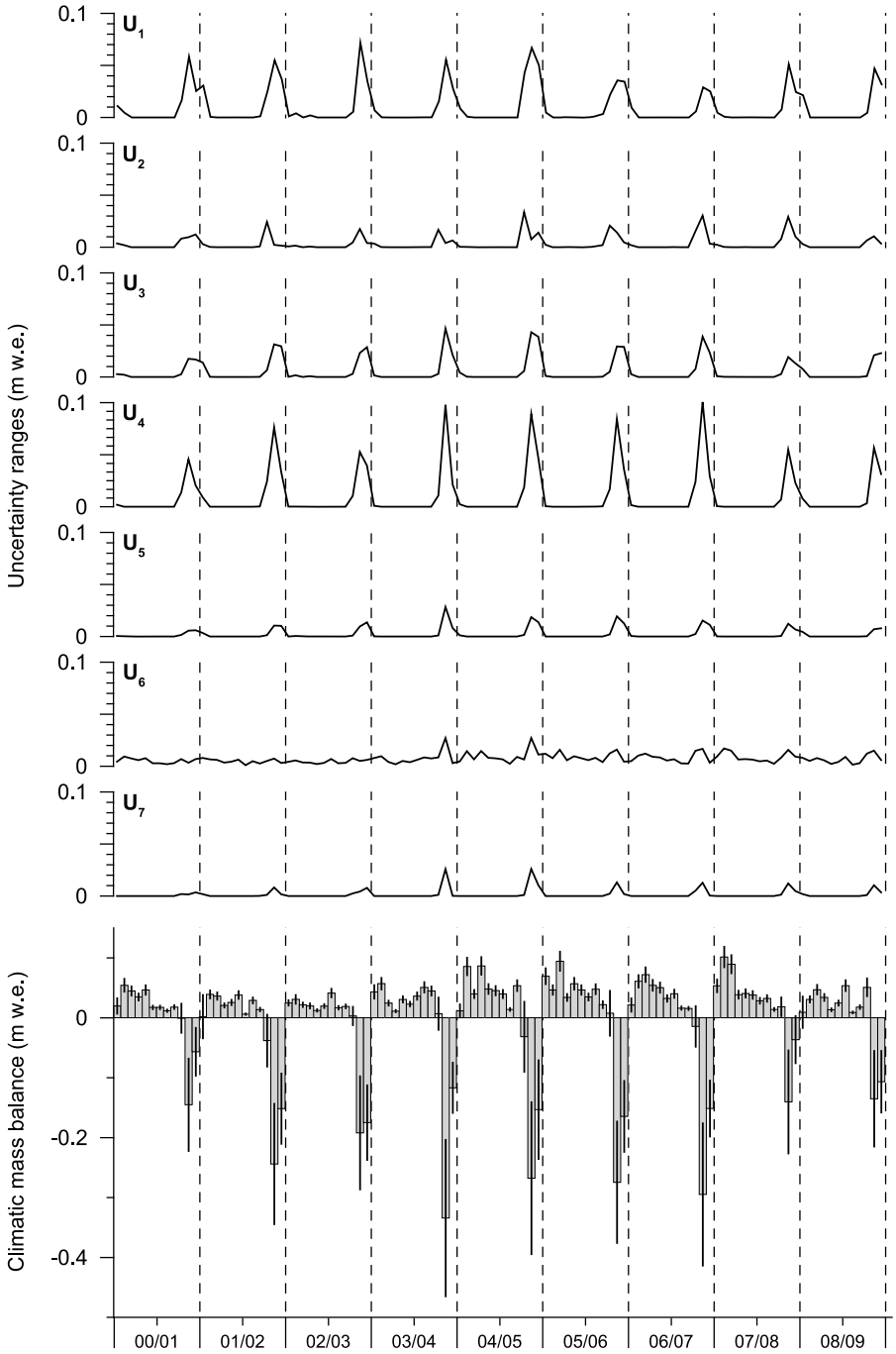

Figure 6. Uncertainties of monthly climatic mass balances. The naming of the individual uncertainty ranges corresponds to Table 3. The black error bars in the bar chart of climatic mass balance represent the overall uncertainty according to equation (11). *x* axis shows mass balance years. Annual subdivisions start September 1.

for the period September 2000 to August 2009 (Figure 7 and Table 4), suggesting roughly balanced conditions. Year-to-year variability is relatively low (<0.5 m) as indicated by the small standard deviation of annual balances (0.15 m w.e.). The mean annual surface ablation rate is -0.58 ± 0.18 m w.e. yr^{-1}, while annual surface accumulation and refreezing rates amount to $+0.40 \pm 0.07$ m w.e. yr^{-1} and $+0.15 \pm 0.04$ m w.e. yr^{-1}, respectively. Hence, on average, approximately one fourth of the surface ablation refreezes. For individual mass balance years, this fraction ranges between 5 and 48% (Figure 7).

[57] The mass balance variability shows a dependency on the North Atlantic Oscillation (NAO, Figure 7). Modeled winter balances correlate significantly ($r = 0.66$, 90% level) with the mean winter NAO (December to February). Posi-

Table 4. Glacier-Wide Modeled Climatic Mass Balance, ELA, and Mass Balance Gradient for the Mass Balance Years 2000/2001 to 2008/2009[a]

Mass Balance Year	Annual Balance (m w.e.)	Winter Balance (m w.e.)	Summer Balance (m w.e.)	Annual Surface Accumulation (m w.e.)	Annual Surface Ablation (m w.e.)	Annual Refreezing (m w.e.)	ELA (m asl)	Gradient (m w.e. km^{-1})
2000/2001	+0.06 ± 0.17	+0.26 ± 0.05	−0.20 ± 0.14	+0.33 ± 0.05	−0.36 ± 0.15	+0.09 ± 0.04	375 ± 18	2.65
2001/2002	−0.22 ± 0.23	+0.21 ± 0.06	−0.43 ± 0.19	+0.29 ± 0.05	−0.55 ± 0.21	+0.03 ± 0.03	457 ± 17	2.91
2002/2003	−0.16 ± 0.18	+0.21 ± 0.04	−0.36 ± 0.17	+0.24 ± 0.04	−0.49 ± 0.16	+0.09 ± 0.04	453 ± 22	2.47
2003/2004	−0.12 ± 0.21	+0.32 ± 0.06	−0.44 ± 0.19	+0.39 ± 0.07	−0.70 ± 0.18	+0.19 ± 0.05	415 ± 19	3.05
2004/2005	−0.03 ± 0.28	+0.42 ± 0.07	−0.45 ± 0.25	+0.51 ± 0.09	−0.78 ± 0.23	+0.24 ± 0.06	383 ± 15	4.16
2005/2006	+0.02 ± 0.22	+0.45 ± 0.08	−0.43 ± 0.19	+0.53 ± 0.09	−0.74 ± 0.22	+0.23 ± 0.06	364 ± 19	3.71
2006/2007	−0.10 ± 0.22	+0.36 ± 0.06	−0.46 ± 0.19	+0.45 ± 0.07	−0.66 ± 0.20	+0.11 ± 0.07	377 ± 18	2.97
2007/2008	+0.28 ± 0.18	+0.44 ± 0.07	−0.16 ± 0.14	+0.51 ± 0.09	−0.45 ± 0.15	+0.21 ± 0.06	283 ± 10	3.19
2008/2009	+0.05 ± 0.18	+0.24 ± 0.05	−0.19 ± 0.14	+0.36 ± 0.06	−0.45 ± 0.16	+0.13 ± 0.03	339 ± 14	2.72
Average	−0.02 ± 0.20	+0.32 ± 0.06	−0.35 ± 0.17	+0.40 ± 0.07	−0.58 ± 0.18	+0.15 ± 0.04	383 ± 17	3.09
Standard Deviation	0.15	0.10	0.13	0.10	0.15	0.08	54	0.54

[a]Annual and seasonal balances are given according to the fixed date system (winter balance, September 1 to May 31; summer balance, June 1 to August 31). Unit is meters water equivalent error ranges are given according to equation (11).

tive NAO conditions have been suggested to coincide with less sea ice in the Barents Sea [*Yamamoto et al.*, 2006], and thus increased precipitation over Svalbard [*Rogers et al.*, 2001], and vice versa. The summer balances in turn anticorrelate significantly ($r = -0.68$, 95% level) with the mean summer NAO (June to August). Sea ice anomalies in the Barents Sea were found to anticorrelate with air temperature anomalies over Svalbard [*Koenigk et al.*, 2009]. Hence, during positive NAO conditions, increased air temperatures are to be expected over Svalbard, and vice versa.

[58] An exceptionally positive annual climatic mass balance (+0.28 ± 0.18 m w.e.) occurred in 2007/2008. This mass balance year is characterized by a highly positive winter NAO (+0.66) and a highly negative summer NAO (−1.27), thus favoring large accumulation and small ablation. However, comparable NAO conditions also occurred during other mass balance years of the study period, and thus other driving forces for the exceptionally positive mass balance have to be considered. *Francis et al.* [2009] found that negative summer sea ice-extent anomalies also coincide with increased precipitation over Svalbard. Hence, the highly positive winter balance (+0.44 ± 0.07 m w.e.) may be attributed to the coincidence of the highly positive winter NAO and the small Arctic sea ice-extent in September 2007. The least negative summer balance (−0.16 ± 0.14 m w.e.) of the entire study period is consistent with the most negative summer NAO (Figure 7), and with transient weather conditions on Nordaustlandet. Several days of heavy snowfall in the first week of August resulted in a deep fresh snow layer (~0.20 m according to own field observations) that effectively increased the surface albedo on the ice cap. Additionally, this led to distinctly reduced ablation sums during the last month of the 2008 ablation season (Figure 6).

[59] The climatic mass balance profiles of Vestfonna show high interannual variability with gradients ranging from 2.47 to 4.16 m w.e. km^{-1} (Figure 8). Modeled annual equilibrium-line altitudes (ELAs) during the nine years range from 283 ± 10 m asl (2007/2008) to 457 ± 17 m asl (2001/2002), with a mean of 383 ± 54 m asl (mean ± one standard deviation). *Hagen et al.* [2003] estimated the ELA of Vestfonna to fluctuate between 400 and 500 m asl during the last decades of the 20th century. However, their estimate refers to surface mass balance and thus does not consider refreezing below the end-of-summer surface. Refreezing has a large impact on the ELA as it tends to shift the ELA

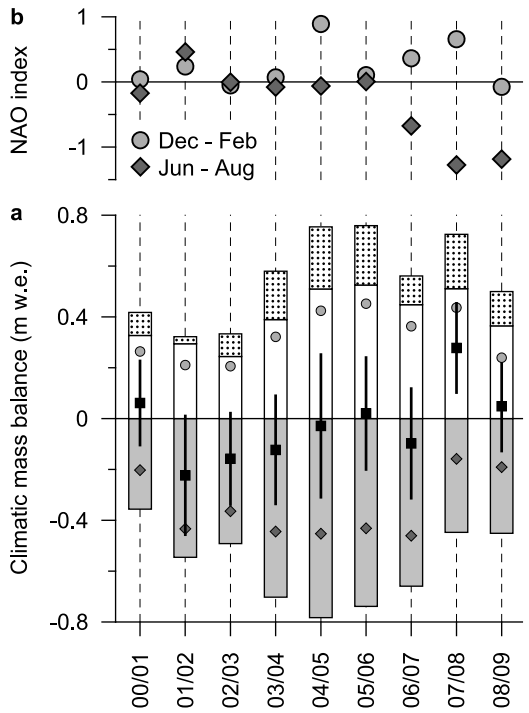

Figure 7. (a) Modeled glacier-wide climatic mass balance of Vestfonna for the mass balance years 2000/2001 to 2008/2009: The bar chart shows annual ablation (gray bars), annual accumulation (white bars), and annual refreezing (dotted). Black squares with error bars represent the annual balances, light gray circles represent the winter balances, and dark gray diamonds represent the summer balances. Each mass balance year lasts from September 1 to August 31. (b) Mean winter (December to February) and mean summer (June to August) NAO (source is the NOAA Climate Prediction Center, http://www.cpc.ncep.noaa.gov).

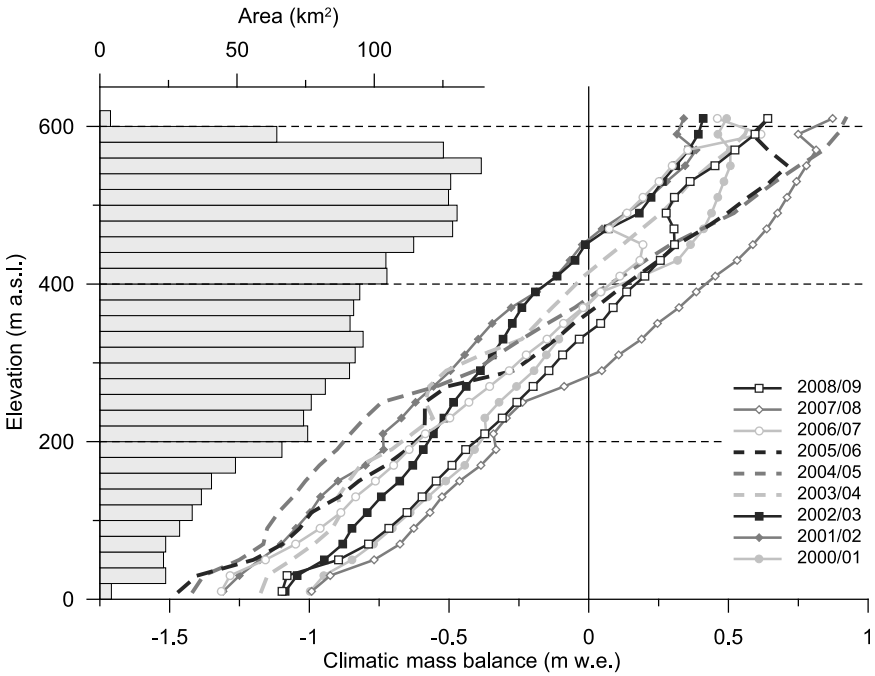

Figure 8. Area-altitude distribution of Vestfonna (bar chart) and mean climatic mass balance profiles for the mass balance years 2000/2001 to 2008/2009. Each mass balance year lasts from September 1 to August 31. Calculations are performed on 20 m altitude bins.

toward higher elevations. As expected, years with more negative climatic balance coincide with lower ELAs, and vice versa.

[60] The spatial variability of climatic mass balance is shown in Figure 9. Mass gain dominated over large parts of the interior of the ice cap, while considerable mass loss occurred throughout the lower marginal areas of the ice cap, in particular on its south facing slopes, as well as Franklinbreen and the northeastern land-terminating parts.

[61] The temporal variability of the modeled climatic mass balances of Vestfonna is in line with findings obtained for Austfonna or the Ny-Ålesund region [*Hagen et al.*, 2003; *Rasmussen and Kohler*, 2007; *Schuler et al.*, 2007]. *Hagen et al.* [2003] suggested Austfonna to be in equilibrium at the beginning of the decade, but for the period from April 2004 to April 2005 *Schuler et al.* [2007] suggested a clearly negative climatic mass balance of −0.32 m w.e. Our results also reveal a quasi-balanced state at the beginning of the decade, but they do not show a distinctly negative mass balance year in the period 2004–2005 (Table 4 and Figure 7). This is likely due to the fact that *Schuler et al.* [2007] modeled accumulation on the basis of the daily precipitation record of the nearest synoptic weather station operated in Ny-Ålesund (180 km southwest of Vestfonna). This record shows a pronounced relative minimum in the period 2004–2005 that is not evident in the ERA-Interim data used in this study. As the ERA-Interim grid point is located much closer to Vestfonna (<50 km SSW), we consider this time series to be distinctly more representative for regional climate on Nordaustlandet than the one from the Ny-Ålesund weather station. The decreasingly negative climatic mass balances of Vestfonna during parts of the decade (Figure 7) are also evident on Austfonna. A comparable pattern was identified in a 5 year surface mass balance time series (2004–2008) of the Eton-/Winsnesbreen basin (northwestern Austfonna) [*Moholdt et al.*, 2010a]. Taken together, it can be concluded that the climatic mass balances of Vestfonna modeled in this study mirror the general mass balance pattern throughout the northern Svalbard archipelago.

7. Conclusion

[62] The climatic mass balance of Vestfonna was calculated for the 9 year period from September 2000 to August 2009 using a temperature-radiation-index mass balance model driven by ERA-Interim air temperature and precipitation data as well as MODIS-based cloud cover and albedo data. Results indicate generally short ablation seasons (3 months) and correspondingly longer accumulation seasons (9 months) over the 9 year period.

[63] Over the nine mass balance years studied Vestfonna shows a mean annual climatic mass balance of −0.02 ± 0.20 m w.e. Mean winter and summer balances amount to +0.32 ± 0.06 and −0.35 ± 0.17 m w.e., respectively, and are found to correlate significantly with NAO conditions. Refreezing plays a major role in the mass budget of the ice cap. On average, roughly one fourth of annual ablation is retained in the firn due to refreezing. However, more measurements and more sophisticated subsurface models are desirable to better ascertain results.

[64] The mean annual ELA is calculated to be 383 ± 54 m asl (mean ± one standard deviation) and thus to a slightly lower altitude than suggested by *Hagen et al.* [2003] for the end of the 20th century. Further studies are needed to

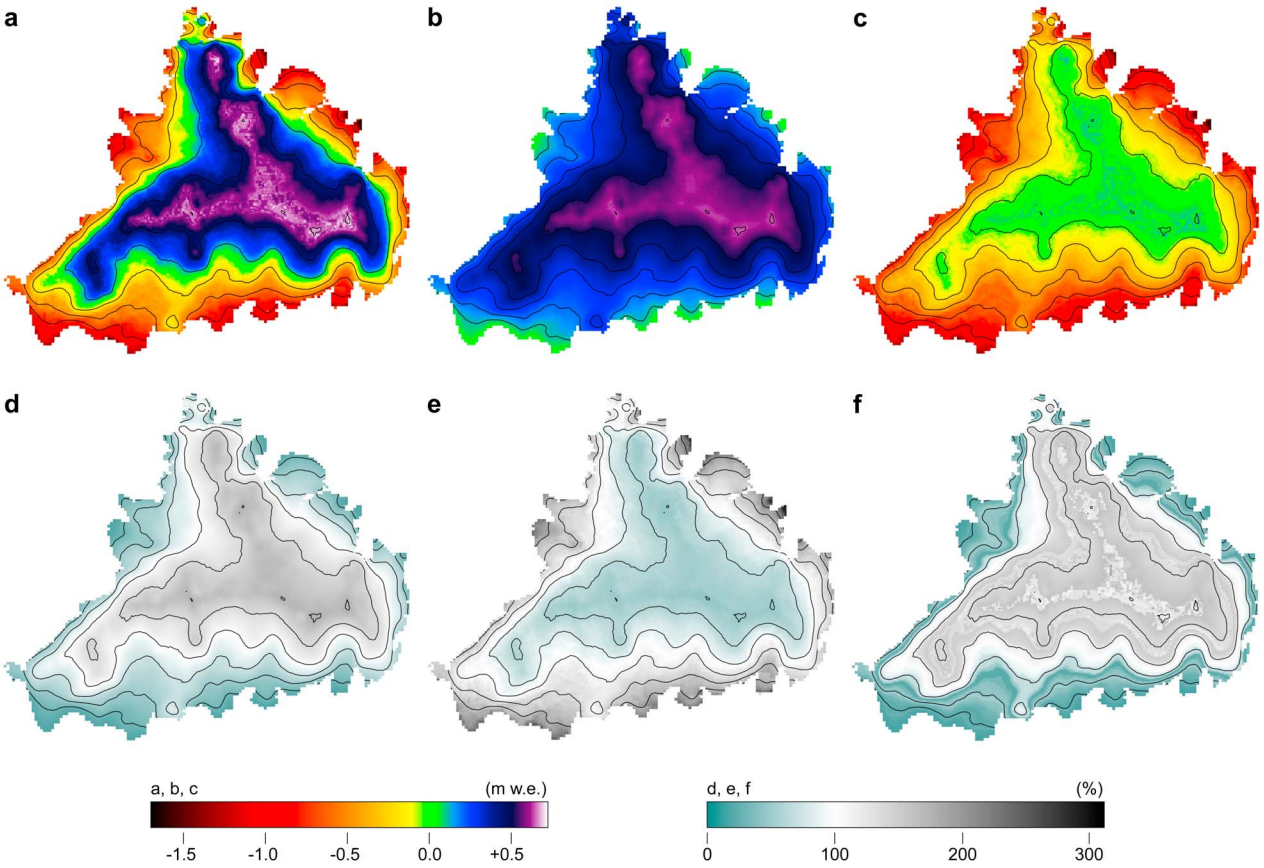

Figure 9. The climatic mass balance of Vestfonna: (a) annual balance, (b) winter balance, and (c) summer balance. (d) Annual accumulation, (e) annual ablation, and (f) annual refreezing presented as deviation from the spatial mean (i.e., as the ratio of specific mass balance components and their glacier-wide means). Each plot shows the averaged pattern of the mass balance years 2000/2001 to 2008/2009. Each mass balance year lasts from September 1 to August 31. Elevation contour spacing is 100 m.

quantify mass loss by calving, in order to arrive at total mass changes of the ice cap.

[65] **Acknowledgments.** This study was carried out under the umbrella of the International Polar Year (IPY) core projects Kinnvika and Glaciodyn and greatly benefited from the logistical sponsorship within IPY Kinnvika in the field. The authors express their gratitude to all people involved in fieldwork during the various field campaigns and acknowledge the Swedish Polar Research Secretariat and R/V *Horyzont II* from the Polish Marine Academy in Gdynia for logistical support. The Nordic Council of Ministers is acknowledged for financial support. The study was funded by grants BR 2105/6–1, SCHE 750/3–1, and SCHN 680/2-1 of the German Research Foundation (DFG). Additional funding was provided by grant 621-2007-3738 of the Swedish Research Council. Comments and suggestions by three anonymous reviewers very much helped to improve the manuscript and are gratefully acknowledged. Bob McNabb is acknowledged for correcting the English.

References

Arendt, A. A., K. A. Echelmeyer, W. D. Harrison, C. S. Lingle, and V. B. Valentine (2002), Rapid wastage of Alaska glaciers and their contribution to rising sea level, *Science*, *297*, 382–386, doi:10.1126/science.1072497.

Bahr, D. B., M. Dyurgerov, and M. F. Meier (2009), Sea-level rise from glaciers and ice caps: A lower bound, *Geophys. Res. Lett.*, *36*, L03501, doi:10.1029/2008GL036309.

Berendes, T. A., D. A. Berendes, R. M. Welch, E. G. Dutton, T. Uttal, and E. E. Clothiaux (2004), Cloud cover comparisons of the MODIS daytime cloud mask with surface instruments at the north slope of Alaska ARM site, *IEEE Trans. Geosci. Remote Sens.*, *42*(11), 2584–2593, doi:10.1109/TGRS.2004.835226.

Bernhardt, F., and H. Philipps (1958), *Die räumliche und zeitliche Verteilung der Einstrahlung, der Ausstrahlung und der Strahlungsbilanz im Meeresniveau, Teil I, Die Einstrahlung*, Akademie Verlag, Berlin.

Berthier, E., E. Schiefer, G. K. C. Clarke, B. Menounos, and F. Rémy (2010), Contribution of Alaskan glaciers to sea-level rise derived from satellite imagery, *Nat. Geosci.*, *3*(2), 92–95, doi:10.1038/ngeo737.

Bevan, S., A. Luckman, T. Murray, H. Sykes, and J. Kohler (2007), Positive mass balance during the late 20th century on Austfonna, Svalbard, revealed using satellite radar interferometry, *Ann. Glaciol.*, *46*, 117–122, doi:10.3189/172756407782871477.

Bevington, R. R. (1969), *Data Reduction and Error Analysis for the Physical Science*, McGraw-Hill, New York.

Braithwaite, R. J., and S. C. B. Raper (2007), Glaciological conditions in seven contrasting regions estimated with the degree-day model, *Ann. Glaciol.*, *46*, 297–302, doi:10.3189/172756407782871206.

Budyko, M. I. (1974), *Climate and Life*, Academic, New York.

Cogley, J. G., et al. (2011), *Glossary of Glacier Mass Balance and Related Terms, IHP-VII Tech. Doc. Hydrol. 86, IACS Contrib. 2*, UNESCO-IHP, Paris.

Corripio, J. G. (2003), Vectorial algebra algorithms for calculating terrain parameters from DEMs and solar radiation modelling in mountainous terrain, *Int. J. Geogr. Inf. Sci.*, *17*(1), 1–23, doi:10.1080/713811744.

Dowdeswell, J. A., and R. L. Collin (1990), Fast-flowing outlet glaciers on Svalbard ice caps, *Geology*, *18*(8), 778–781, doi:10.1130/0091-7613(1990)018<0778:FFOGOS>2.3.CO;2.

Dumanskaya, I. O. (2008), Applying the dynamical-statistical method of calculations of the ice redistribution in the White Sea for the solution

of climatic and prognostic problems, *Oceanology, Engl. Transl.*, *48*(1), 15–22, doi:10.1134/S0001437008010037.
Emelyanov, Y. N., and V. G. Konovalov (1975), Estimation of total ablation on Central Asian glaciers, *IAHS-AISH Publ.*, *104*, 99–105.
Førland, E. J., and I. Hanssen-Bauer (2003), Past and future climate variations in the Norwegian Arctic: Overview and novel analysis, *Polar Res.*, *22*(2), 113–124, doi:10.1111/j.1751-8369.2003.tb00102.x.
Førland, E. J., I. Hanssen-Bauer, and P. Ø. Nordli (1997), Climate statistics and long term series of temperatures and precipitation at Svalbard and Jan Mayen, *DNMI Rep. 21-97*, Det Norske Meteorologisk Institutt, Oslo.
Francis, J. A., W. Chan, D. J. Leathers, J. R. Miller, and D. E. Veron (2009), Winter Northern Hemisphere weather patterns remember summer Arctic sea-ice extent, *Geophys. Res. Lett.*, *36*, L07503, doi:10.1029/2009GL037274.
Goodison, B. E., H. L. Ferguson, and G. A. McKay (1981), Measurement and data analysis, in *Handbook of Snow*, edited by D. M. Gray and D. H. Male, pp. 191–274, Pergamon, Toronto.
Greuell, W., and J. Oerlemans (2005), Validation of AVHRR- and MODIS-derived albedos of snow and ice surfaces by means of helicopter measurements, *J. Glaciol.*, *51*(172), 37–48, doi:10.3189/172756505781829575.
Hagen, J. O., K. Melvold, F. Pinglot, and J. A. Dowdeswell (2003), On the net mass balance of the glaciers and ice caps in Svalbard, Norwegian Arctic, *Arct. Antarct. Alp. Res.*, *35*(2), 264–270, doi:10.1657/1523-0430(2003)035[0264:OTNMBO]2.0.CO;2.
Hall, D. K., and G. A. Riggs (2007), Accuracy assessment of the MODIS snow products, *Hydrol. Processes*, *21*(12), 1534–1547, doi:10.1002/hyp.6715.
Hall, D. K., G. A. Riggs, V. V. Salomonson, N. E. DiGirolamo, and K. J. Bayr (2002), MODIS snow-cover products, *Remote Sens. Environ.*, *83*(1–2), 181–194, doi:10.1016/S0034-4257(02)00095-0.
Hanssen-Bauer, I., and E. J. Førland (1998), Long-term trends in precipitation and temperature in the Norwegian Arctic: Can they be explained by changes in atmospheric circulation patterns?, *Clim. Res.*, *10*(2), 143–153, doi:10.3354/cr010143.
Hock, R. (2003), Temperature index melt modelling in mountain areas, *J. Hydrol.*, *282*(1–4), 104–115, doi:10.1016/S0022-1694(03)00257-9.
Huth, R. (1999), Statistical downscaling in central Europe: Evaluation of methods and potential predictors, *Clim. Res.*, *13*, 91–101, doi:10.3354/cr013091.
Huth, R., J. Kyselý, and M. Dubrovský (2001), Time structure of observed, GCM-simulated, downscaled, and stochastically generated daily temperature series, *J. Clim.*, *14*(20), 4047–4061, doi:10.1175/1520-0442(2001)014<4047:TSOOGS>2.0.CO;2.
Iqbal, M. (1983), *An Introduction to Solar Radiation*, Academic, New York.
Kääb, A. (2008), Glacier volume changes using ASTER satellite stereo and ICESat GLAS laser altimetry. A test study on Edgeøya, eastern Svalbard, *IEEE Trans. Geosci. Remote Sens.*, *46*(10), 2823–2830, doi:10.1109/TGRS.2008.2000627.
Karl, T. R., W. C. Wang, M. E. Schlesinger, R. W. Knight, and D. Portman (1990), A method of relating general circulation model simulated climate to observed local climate. Part I: Seasonal statistics, *J. Clim.*, *3*(10), 1053–1079, doi:10.1175/1520-0442(1990)003<1053:AMORGC>2.0.CO;2.
Kaser, G., J. G. Cogley, M. B. Dyurgerov, M. F. Meier, and A. Ohmura (2006), Mass balance of glaciers and ice caps: Consensus estimates for 1961–2004, *Geophys. Res. Lett.*, *33*, L19501, doi:10.1029/2006GL027511.
Koenigk, T., U. Mikolajewicz, J. H. Jungclaus, and A. Kroll (2009), Sea ice in the Barents Sea: Seasonal to interannual variability and climate feedbacks in a global coupled model, *Clim. Dyn.*, *32*, 1119–1138, doi:10.1007/s00382-008-0450-2.
Kohler, J., T. D. James, T. Murray, C. Nuth, O. Brandt, N. E. Barrand, H. F. Aas, and A. Luckman (2007), Acceleration in thinning rate on western Svalbard glaciers, *Geophys. Res. Lett.*, *34*, L18502, doi:10.1029/2007GL030681.
Kondratyev, K. Y. (1969), *Radiation in the Atmosphere*, Academic, San Diego, Calif.
Linke, F. (1961), Die Sonnenstrahlung und ihre Schwächung in der Atmosphäre, in *Handbuch Geophysik*, vol. 8, edited by F. Linke and F. Möller, pp. 239–338, Borntraeger, Berlin.
Meier, M. F., et al. (2007), Glaciers dominate eustatic sea-level rise in the 21st century, *Science*, *317*, 1064–1067, doi:10.1126/science.1143906.
Moholdt, G., J. O. Hagen, T. Eiken, and T. V. Schuler (2010a), Geometric changes and mass balance of the Austfonna ice cap, Svalbard, *Cryosphere*, *4*(1), 21–34, doi:10.5194/tc-4-21-2010.
Moholdt, G., C. Nuth, J. O. Hagen, and J. Kohler (2010b), Recent elevation changes of Svalbard glaciers derived from ICESat laser altimetry, *Remote Sens. Environ.*, *114*(11), 2756–2767, doi:10.1016/j.rse.2010.06.008.
Mölg, T., C. Georges, and G. Kaser (2003), The contribution of increased incoming shortwave radiation to the retreat of the Rwenzori Glaciers, East Africa, during the 20th century, *Int. J. Climatol.*, *23*(3), 291–303, doi:10.1002/joc.877.
Möller, M., and C. Schneider (2010), Calibration of glacier volume-area relations from surface extent fluctuations and application to future glacier change, *J. Glaciol.*, *56*(195), 33–40, doi:10.3189/002214310791190866.
Möller, M., C. Schneider, and R. Kilian (2007), Glacier change and climate forcing in recent decades at Gran Campo Nevado, southernmost Patagonia, *Ann. Glaciol.*, *46*, 136–144, doi:10.3189/172756407782871530.
Möller, M., R. Möller, É. Beaudon, O.-P. Mattila, R. Finkelnburg, M. Braun, B. Luks, U. Jonsell, D. Scherer, and C. Schneider (2011), Snowpack characteristics of Vestfonna and De Geerfonna (Nordaustlandet, Svalbard)–A spatiotemporal analysis based on multiyear snow pit data, *Geogr. Ann.*, in press.
Moritz, R. E., C. M. Bitz, and E. J. Steig (2002), Dynamics of recent climate change in the Arctic, *Science*, *297*, 1497–1502, doi:10.1126/science.1076522.
Nuth, C., G. Moholdt, J. Kohler, J. O. Hagen, and A. Kääb (2010), Svalbard glacier elevation changes and contribution to sea level rise, *J. Geophys. Res.*, *115*, F01008, doi:10.1029/2008JF001223.
Ohmura, A. (2001), Physical basis for the temperature-based melt-index method, *J. Appl. Meteorol.*, *40*(4), 753–761, doi:10.1175/1520-0450(2001)040<0753:PBFTTB>2.0.CO;2.
Ørbæk, J. B., V. Hisdal, and L. E. Svaasand (1999), Radiation climate variability in Svalbard: Surface and satellite observations, *Polar Res.*, *18*(2), 127–134, doi:10.1111/j.1751-8369.1999.tb00284.x.
Palosuo, E. (1987), Ice layers and superimposition of ice on the summit and slope of Vestfonna, Svalbard, *Geogr. Ann. Ser. A*, *69*(2), 289–296, doi:10.2307/521189.
Paterson, W. S. B. (1994), *The Physics of Glaciers*, Elsevier, Oxford, U. K.
Pellicciotti, F., B. Brock, U. Strasser, P. Burlando, M. Funk, and J. Corripio (2005), An enhanced temperature-index glacier melt model including the shortwave radiation balance: Development and testing for Haut Glacier d'Arolla, Switzerland, *J. Glaciol.*, *51*(175), 573–587, doi:10.3189/172756505781829124.
Przybylak, R. (2000), Temporal and spatial variation of surface air temperature over the period of instrumental observations in the Arctic, *Int. J. Climatol.*, *20*(6), 587–614, doi:10.1002/(SICI)1097-0088(200005)20:6<587::AID-JOC480>3.0.CO;2-H.
Przybylak, R. (2007), Recent air temperature changes in the Arctic, *Ann. Glaciol.*, *46*, 316–324, doi:10.3189/172756407782871666.
Raper, S. C. B., and R. J. Braithwaite (2006), Low sea level rise projections from mountain glaciers and ice caps under global warming, *Nature*, *439*, 311–313, doi:10.1038/nature04448.
Rasmussen, L. A., and J. Kohler (2007), Mass balance of three Svalbard glaciers reconstructed back to 1948, *Polar Res.*, *26*, 168–174, doi:10.1111/j.1751-8369.2007.00023.x.
Reeh, N. (1991), Parameterization of melt rate and surface temperature on the Greenland ice sheet, *Polarforschung*, *59*(3), 113–128.
Rigor, I. G., R. L. Colony, and S. Martin (2000), Variations in surface air temperature observations in the Arctic, 1979–97, *J. Clim.*, *13*(5), 896–914, doi:10.1175/1520-0442(2000)013<0896:VISATO>2.0.CO;2.
Rinke, A., and K. Dethloff (2008), Simulated circum-Arctic climate changes by the end of the 21st century, *Global Planet. Change*, *62*(1–2), 173–186, doi:10.1016/j.gloplacha.2008.01.004.
Rogers, A. N., D. H. Bromwich, E. N. Sinclair, and R. I. Cullather (2001), The atmospheric hydrologic cycle over the Arctic Basin from reanalysis. Part II: Interannual variability, *J. Clim.*, *14*(11), 2414–2429, doi:10.1175/1520-0442(2001)014<2414:TAHCOT>2.0.CO;2.
Schuler, T. V., E. Loe, A. Taurisano, T. Eiken, J. O. Hagen, and J. Kohler (2007), Calibrating a surface mass-balance model for Austfonna ice cap, Svalbard, *Ann. Glaciol.*, *46*, 241–248, doi:10.3189/172756407782871783.
Schüttemeyer, D., C. Schillings, A. F. Moene, and H. A. R. de Bruin (2007), Satellite-Based Actual Evapotranspiration over Drying Semiarid Terrain in West Africa, *J. Appl. Meteorol. Climatol.*, *46*(1), 97–111, doi:10.1175/JAM2444.1.
Stroeve, J. C., J. E. Box, and T. Haran (2006a), Evaluation of the MODIS (MOD10A1) daily snow albedo product over the Greenland ice sheet, *Remote Sens. Environ.*, *105*(2), 155–171, doi:10.1016/j.rse.2006.06.009.
Stroeve, J., T. Markus, W. N. Meier, and J. Miller (2006b), Recent changes in the Arctic melt season, *Ann. Glaciol.*, *44*, 367–374, doi:10.3189/172756406781811583.
Strozzi, T., A. Kouraev, A. Wiesmann, U. Wegmüller, A. Sharov, and C. Werner (2008), Estimation of Arctic glacier motion with satellite L-band SAR data, *Remote Sens. Environ.*, *112*(3), 636–645, doi:10.1016/j.rse.2007.06.007.
Taurisano, A., T. V. Schuler, J. O. Hagen, T. Eiken, E. Loe, K. Melvold, and J. Kohler (2007), The distribution of snow accumulation across the Austfonna ice cap, Svalbard: Direct measurements and modelling, *Polar Res.*, *26*(1), 7–13, doi:10.1111/j.1751-8369.2007.00004.x.

Uppala, S. M., et al. (2005), The ERA-40 re-analysis, *Q. J. R. Meteorol. Soc.*, *131*, 2961–3012, doi:10.1256/qj.04.176.

von Storch, H. (1999), On the use of "inflation" in statistical downscaling, *J. Clim.*, *12*(12), 3505–3506, doi:10.1175/1520-0442(1999)012<3505:OTUOII>2.0.CO;2.

Wald, L., et al. (2002), SoDa: A project for the integration and exploitation of networked solar radiation databases, in *Environmental Communication in the Information Society*, edited by W. Pillmann and K. Tochtermann, pp. 713–720, Int. Soc. for Environ. Prot., Vienna.

Wang, X., and C. S. Zender (2010), MODIS snow albedo bias at high solar zenith angles relative to theory and to in situ observations in Greenland, *Remote Sens. Environ.*, *114*(3), 563–575, doi:10.1016/j.rse.2009.10.014.

Wang, X., H. Xie, and T. Liang (2008), Evaluation of MODIS snow cover and cloud mask and its application in Northern Xinjiang, China, *Remote Sens. Environ.*, *112*(4), 1497–1513, doi:10.1016/j.rse.2007.05.016.

Wu, X., M. B. Heflin, H. Schotman, B. L. A. Vermeersen, D. Dong, R. S. Gross, E. R. Ivins, A. W. Moore, and S. E. Owen (2010), Simultaneous estimation of global present-day water transport and glacial isostatic adjustment, *Nat. Geosci.*, *3*(9), 642–646, doi:10.1038/ngeo938.

Yamamoto, K., Y. Tachibana, M. Honda, and J. Ukita (2006), Intra-seasonal relationship between the Northern Hemisphere sea ice variability and the North Atlantic Oscillation, *Geophys. Res. Lett.*, *33*, L14711, doi:10.1029/2006GL026286.

M. Braun and R. Hock, Geophysical Institute, University of Alaska Fairbanks, 903 Koyukuk Dr., Fairbanks, AK 99775, USA.

R. Finkelnburg and D. Scherer, Department of Ecology, Technische Universität Berlin, Rothenburgstr. 12, D-12165 Berlin, Germany.

U. Jonsell, Swedish Polar Research Secretariat, PO Box 50003, SE-104 05 Stockholm, Sweden.

M. Möller and C. Schneider, Department of Geography, RWTH Aachen University, D-52062 Aachen, Germany. (marco.moeller@geo.rwth-aachen.de)

V. A. Pohjola, Department of Earth Sciences, Uppsala University, Villavägen 16, SE-752 36, Uppsala, Sweden.